

## A FLASH IN THE DARK: UVES VERY LARGE TELESCOPE HIGH-RESOLUTION SPECTROSCOPY OF GAMMA-RAY BURST AFTERGLOWS<sup>1</sup>

F. FIORE,<sup>2</sup> V. D'ELIA,<sup>2</sup> D. LAZZATI,<sup>3,4</sup> R. PERNA,<sup>4,5</sup> L. SBORDONE,<sup>2,6</sup> G. STRATTA,<sup>2,7</sup>  
E. J. A. MEURS,<sup>8</sup> P. WARD,<sup>8</sup> L. A. ANTONELLI,<sup>2</sup> G. CHINCARINI,<sup>9</sup> S. COVINO,<sup>10</sup>  
A. DI PAOLA,<sup>2</sup> A. FONTANA,<sup>2</sup> G. GHISELLINI,<sup>10</sup> G. ISRAEL,<sup>2</sup> F. FRONTERA,<sup>11</sup>  
G. MARCONI,<sup>2,6</sup> L. STELLA,<sup>2</sup> M. VIETRI,<sup>12</sup> AND F. ZERBI<sup>10</sup>

Received 2004 May 4; accepted 2005 January 31

### ABSTRACT

We present the first high-resolution ( $R = 20,000\text{--}45,000$ , corresponding to  $14\text{ km s}^{-1}$  at  $4200\text{ \AA}$  to  $6.6\text{ km s}^{-1}$  at  $9000\text{ \AA}$ ) observations of the optical afterglow of gamma-ray bursts. GRB 020813 and GRB 021004 were observed by UVES at the Very Large Telescope 22.19 and 13.52 hr after the trigger, respectively. These spectra show that the interstellar matter of the GRB host galaxies is complex, with many components contributing to each main absorption system, and spans a total velocity range of up to about  $3000\text{ km s}^{-1}$ . Several narrow components are resolved down to a width of a few tens of  $\text{km s}^{-1}$ . In the case of GRB 021004 we detected both low- and high-ionization lines. Combined with photoionization results obtained with CLOUDY, the ionization parameters of the various systems are consistent with a remarkably narrow range with no clear trend with system velocity. This can be interpreted as due to density fluctuations on top of a regular  $R^{-2}$  wind density profile.

*Subject headings:* cosmology: observations — galaxies: abundances — galaxies: ISM — gamma rays: bursts

*Online material:* color figures

### 1. INTRODUCTION

For a few hours after their onset, gamma-ray bursts (GRBs) are the brightest beacons in the far universe, offering a superb opportunity to investigate both GRB physics and high-redshift galaxies. Tens of minutes after a GRB, its optical afterglow can be as bright as magnitude 13–15; a few hours later a magnitude of 16–19 is often achieved. Bright examples are the cases of GRB 990123 ( $z = 1.600$ ), for which the reverse shock reached  $R = 9\text{--}10\text{ mag}$  1 minute after the GRB and the optical afterglow reached  $R = 14\text{ mag}$  12 minutes after the GRB (e.g., Akerlof et al. 1999; Galama et al. 1999), and GRB 030329 ( $z = 0.1685$ ), for which the optical afterglow reached  $R = 12.7\text{ mag}$  at 1.5 hr from the GRB and decreased to  $R = 19\text{ mag}$  after  $\sim 10$  days (e.g., Price et al. 2003; Stanek et al. 2003). High-resolution (a few tens of  $\text{km s}^{-1}$  in the optical band), high-quality (signal-to-noise ratio  $>10$  per resolution element) spectra can therefore be gathered, provided that the afterglow is observed rapidly by 8 m class telescopes. Since GRBs are associated with the collapse of

massive stars (see Woosley 1993; Paczyński 1998; MacFadyen & Woosley 1999; Vietri & Stella 1998 for theoretical reasons and Galama et al. 1998; Stanek et al. 2003; Hjorth et al. 2003; Della Valle et al. 2003 for observational reasons), this is expected to open a new window in the study of the environment in which intermediate- to high-redshift star formation occurs and, in particular, on the physical, chemical, and dynamical state of the interstellar matter (ISM) of the GRB host galaxies.

The study of  $z \gtrsim 1$  galaxies has so far mostly relied on Lyman break galaxies (LBGs) at  $z = 3\text{--}4$  (see, e.g., Steidel et al. 1999) and galaxies that happen to be along the line of sight to bright background QSOs. Some of these systems are associated with damped Ly $\alpha$  systems (DLAs; see, e.g., Pettini et al. 1997). However, LBGs are characterized by pronounced star formation, and their inferred chemical abundances may be related to these regions rather than being representative of typical high- $z$  galaxies. Metal line systems associated with DLAs along the line of sight to quasars probe mainly galaxy haloes, rather than their bulges or disks. Furthermore, it is not clear whether galaxies associated with DLAs are truly representative of the whole high- $z$  galaxy population. GRB afterglows provide an independent tool for studying the ISM of high- $z$  galaxies. Savaglio et al. (2003) studied the metal abundances in three GRB host galaxies using low-medium resolution spectroscopy and a curve-of-growth analysis. They found metal column densities higher than in QSO-DLAs and a strong inverse correlation between [Si/Zn], [Cr/Zn], and [Fe/Zn] and the Zn column density, indicating a dense environment and large dust depletion. On the other hand, Vreeswijk et al. (2004) found indications for a relatively low metallicity and low dust content in the ISM of the  $z = 3.372$  host galaxy of GRB 030323, using FORS2 low- and intermediate-resolution spectroscopy. Again using a curve-of-growth analysis, and taking advantage of ultradeep Gemini multiobject spectrograph observations, Savaglio et al. (2004) studied the ISM of a sample of faint  $K$ -band-selected galaxies at  $1.4 < z < 2.0$ , finding Mg II and Fe II abundances much higher than in QSO-DLAs and

<sup>1</sup> Based on observations collected at the European Southern Observatory, ESO, the VLT/Kueyen telescope, Paranal, Chile, in the framework of programs 69.A-0516(B) and 70.A-0599(B).

<sup>2</sup> INAF-Osservatorio Astronomico di Roma, Via Frascati 33, I-00044 Monteporzio Catone, Italy.

<sup>3</sup> Institute of Astronomy, University of Cambridge, Madingley Road, Cambridge, UK.

<sup>4</sup> Department of Astrophysical and Planetary Science, University of Colorado, Boulder, CO 80309.

<sup>5</sup> Princeton University Observatory, Princeton, NJ 08544-1001.

<sup>6</sup> European Southern Observatory, Casilla 19001, Santiago, Chile.

<sup>7</sup> Dipartimento di Fisica, Università di Roma La Sapienza, Rome, Italy.

<sup>8</sup> Dunsink Observatory, Castleknock, Dublin 15, Ireland.

<sup>9</sup> Università di Milano Bicocca, Piazza della Scienza 3, 20126 Milan, Italy.

<sup>10</sup> INAF, Osservatorio Astronomico di Brera, via E. Bianchi 46, 23807 Merate (LC), Italy.

<sup>11</sup> Dipartimento di Fisica, Università di Ferrara, via Paradiso 12, 44100 Ferrara, Italy.

<sup>12</sup> Scuola Normale Superiore, I-56100 Pisa, Italy.

TABLE 1  
JOURNAL OF OBSERVATIONS

DATE (UT)	DICHROIC	CENTRAL WAVELENGTH (Å)		SLIT (arcsec)	SEEING (arcsec)	EXPOSURE (minutes)	TIME SINCE GRB (hr)
		Blue Arm	Red Arm				
2002 Aug 14 00:55:25 .....	1	3460	5800	1	≤1	60	22.19
2002 May 10 01:37:37 .....	2	4370	8600	1	≤1	30	13.52
2002 May 10 02:10:53 .....	1	3460	5800	1	≤1	30	14.08
2002 May 10 04:09:54 .....	1	3460	5800	1	≤1	60	16.06

similar to those in GRB host galaxies. A much better job can be done with high-resolution ( $R > 20,000$ ) observations because (1) lines can be separated, (2) metal column densities can be measured through a fit to the line profile, (3) fainter lines can be measured, and (4) information on the gas dynamics in the GRB host galaxies can be derived. Furthermore, as suggested by the comparison of the Vreeswijk et al. (2004) and the Savaglio et al. (2004) studies, GRB afterglows allow us to probe galaxy ISM at much higher redshifts than even ultradeep, standard galaxy spectroscopy, such as the Gemini Deep Deep Survey.

For all these reasons we started a pilot program to observe bright GRB afterglows of promptly localized GRBs with UVES at the Very Large Telescope (VLT). The program has been conceived and designed to make full use of the GRB afterglows discovered by the GRB-dedicated *Swift* mission, launched on 2004 November 20.<sup>13</sup> *Swift* will provide GRB positions ( $<4'$  precision) in  $<10$  s, X-ray afterglow positions ( $3''$  precision) in  $<100$  s, and an optical finding chart in  $<300$  s, with a few arcseconds to subarcsecond position accuracy, thus revolutionizing fast-response multiwavelength studies of GRBs.

This article concentrates on high-resolution spectroscopy of two GRB afterglows. The *HETE-2* FREGATE, WXM, and SXC instruments detected GRB 021004 on 2002 October 4 12:06:13.57 UT (Shirasaki et al. 2002) and GRB 020813 on 2002 August 13 02:44:19.17 UT (Villasenor et al. 2002). The WXM flight localization software produced a reliable and relatively accurate position 49 s after the burst for GRB 021004 (error box of  $30'$  radius) and 4 minutes after the burst for GRB 020813 (error box of  $14'$  radius). Bright optical counterparts were identified 10 minutes and 1.9 hr after the triggers by Fox et al. (2002, 2003) and Fox et al. (2002), respectively. Ground analysis of the *HETE-2* data performed a few hours after each GRB improved the localization of the event, providing error boxes of  $2'$  and  $1'$  radius, respectively. UVES observations started 13.52 hr after the GRB 021004 trigger (Savaglio et al. 2002) and 22.19 hr after the GRB 020813 trigger (Fiore et al. 2002).

Optical low- to intermediate-resolution spectroscopy of the afterglow of GRB 021004 was obtained by Møller et al. (2003), Mirabal et al. (2003), Matheson et al. (2003), and Schaefer et al. (2003). One of the main conclusion of these works is that density fluctuations on top of a regular wind density profile are able to explain both the presence of strong, blueshifted, high-ionization absorption-line systems and irregularities in the optical light curve. Schaefer et al. (2003) propose a scenario in which a clumpy wind originates from a massive star progenitor (a Wolf-Rayet star), while Mirabal et al. (2003) suggest that the ionized absorption takes place in a fragmented shell nebula around the GRB progenitor. Optical spectropolarimetry of the afterglow of GRB 020813 has been presented by Barth et al. (2003), who report

the detection of strong absorption systems at  $z = 1.223$  and  $1.255$ . A further analysis of the Keck LRIS spectrum is presented by Savaglio et al. (2004). The present paper reports the results of higher resolution spectroscopy of both afterglows.

Both GRBs were observed in the X-rays too by the *Chandra* High Energy Transmission Grating System, which has a resolution of  $\sim 1000$  at 1 keV (Butler et al. 2003 and references therein). Both observations lasted about 80 ks and started 21 and 20 hr after the GRB event for GRB 020813 and GRB 021004, respectively. Fading X-ray afterglows were detected in both cases with decay indices of  $-1.38 \pm 0.06$  and  $-0.9 \pm 0.1$ , consistent with the values reported for the optical afterglows by Covino et al. (2003) and Holland et al. (2003). The time-averaged fluxes were  $2.2 \times 10^{-12}$  and  $6.3 \times 10^{-13}$  ergs  $\text{cm}^{-2} \text{s}^{-1}$ , respectively. The X-ray spectra are consistent with power laws of energy index of  $-0.85 \pm 0.04$  and  $-1.01 \pm 0.08$  reduced at low energy by Galactic column density (which is rather high in the direction of GRB 020813,  $N_{\text{HGal}} = 7.5 \times 10^{20} \text{ cm}^{-2}$ , and is  $N_{\text{HGal}} = 4.2 \times 10^{20} \text{ cm}^{-2}$  in the direction of GRB 021004). The upper limits to the rest-frame X-ray-absorbing column are of the order of a few times  $10^{20}$  in both cases. Butler et al. (2003) report the detection of an emission line at 1.3 keV at the  $3.3 \sigma$  confidence level, interpreted as an S XVI Ly $\alpha$  line blueshifted by  $0.12c$ .

## 2. OBSERVATIONS AND DATA REDUCTION

In the framework of ESO programs 69.A-0516 and 70.A-0599 we observed the afterglows of GRB 020813 and GRB 021004 with the high-resolution UV-visual echelle spectrograph (UVES; Dekker et al. 2000), mounted at the VLT UT2 telescope. Table 1 gives the log of the observations used in this paper. A further 1 hr dichroic 1 observation is available in the ESO archive, but we were not able to extract a reliable spectrum from this observation, which has therefore been discarded. In order to maximize the signal-to-noise ratio the CCD was rebinned to  $2 \times 2$  pixels. The data reduction has been performed using the UVES pipeline.<sup>14</sup> The final useful spectra extend from  $\sim 4250$

<sup>14</sup> See <http://www.eso.org/observing/dfo/quality/UVES/pipeline>.

TABLE 2  
SIGNAL-TO-NOISE RATIO

Wavelength (Å)	2002 Aug 14 00 hr	2002 May 10 01–02 hr	2002 May 10 04 hr
4250.....	...	3.6	...
5000.....	4.7	5.9	9.3
6000.....	5.6	5.4	11.2
7000.....	5.9	9.8	10.2
7800.....	...	6.8	...
9250.....	...	2.9	...

<sup>13</sup> See <http://swift.gsfc.nasa.gov>.

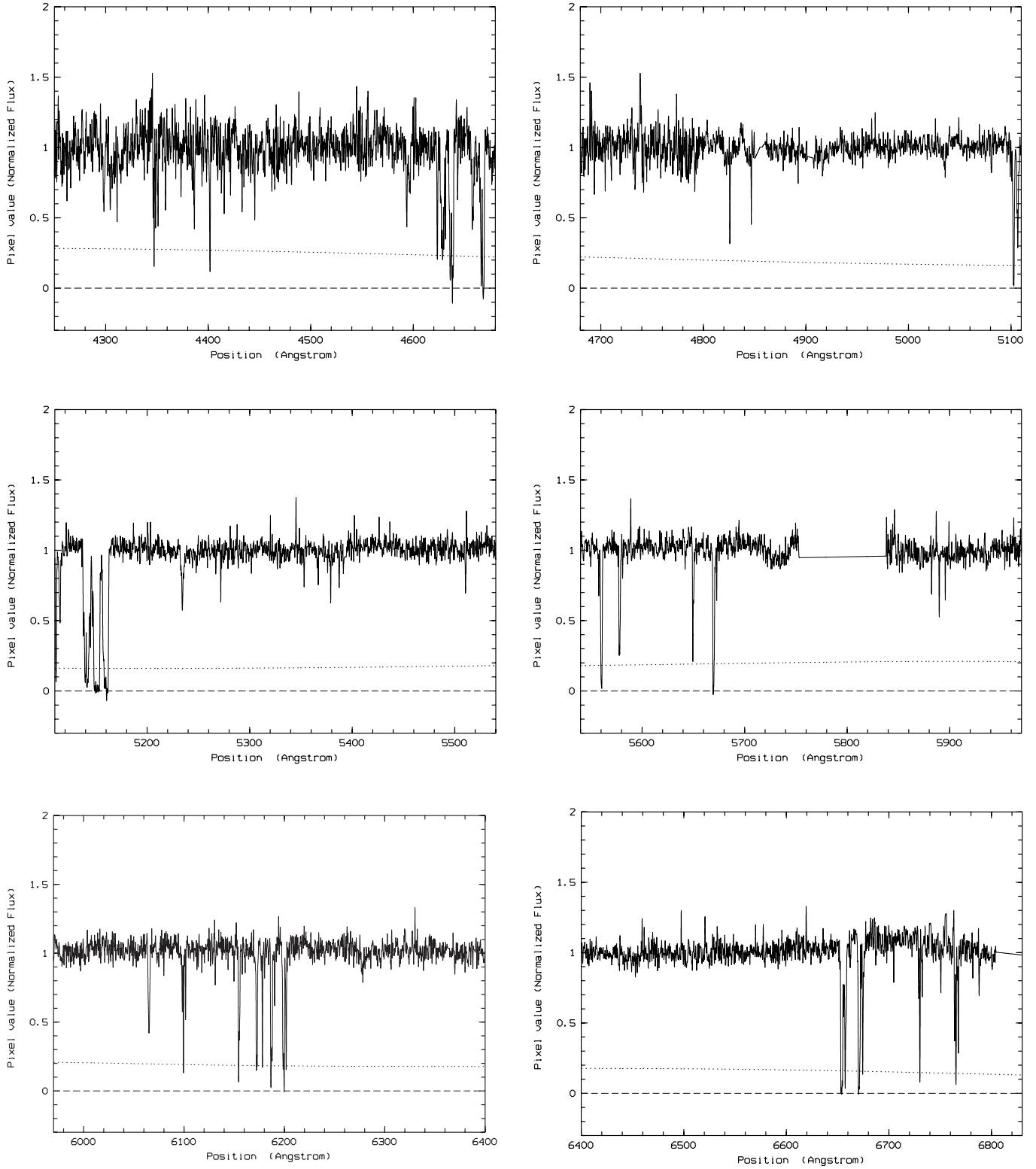


FIG. 1.—UVES spectrum of the GRB 021004 afterglow smoothed with a Gaussian function with  $\sigma = 1.5$  pixels. The dotted line is the error spectrum.

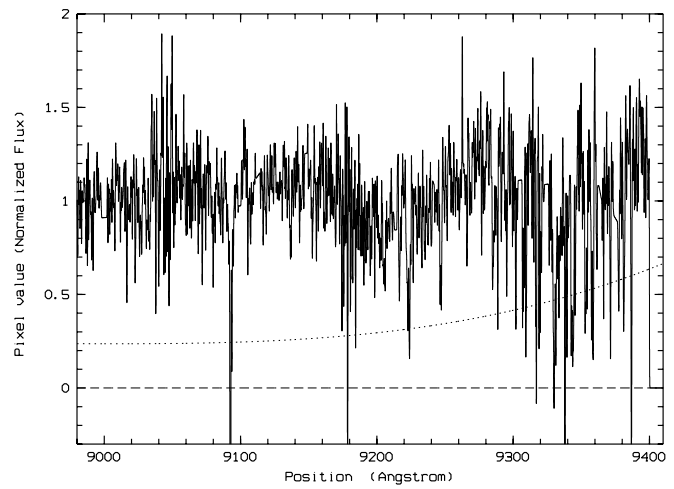
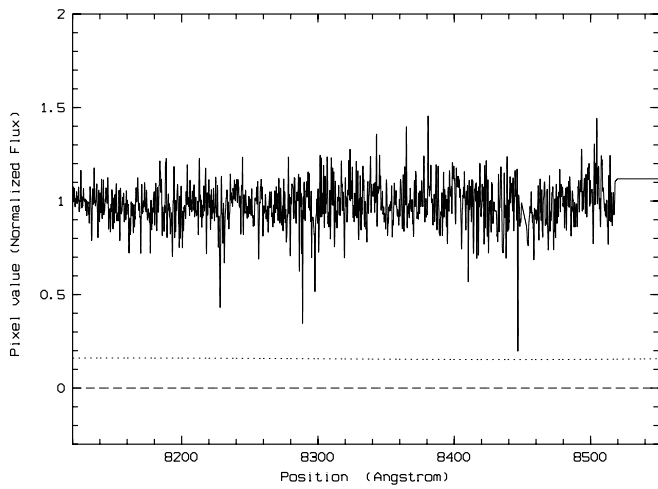
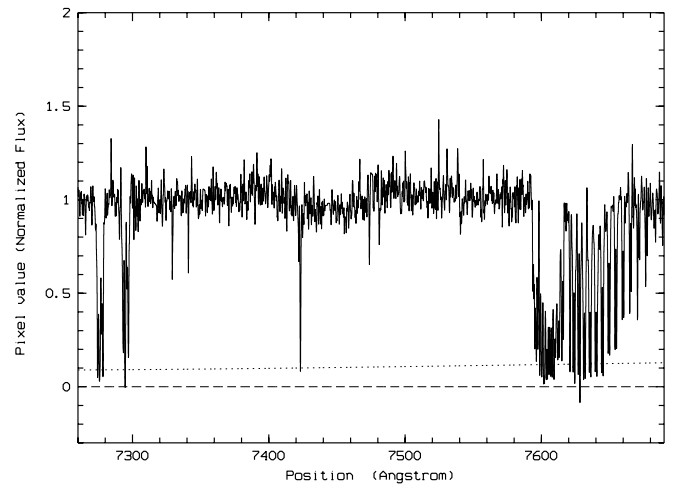
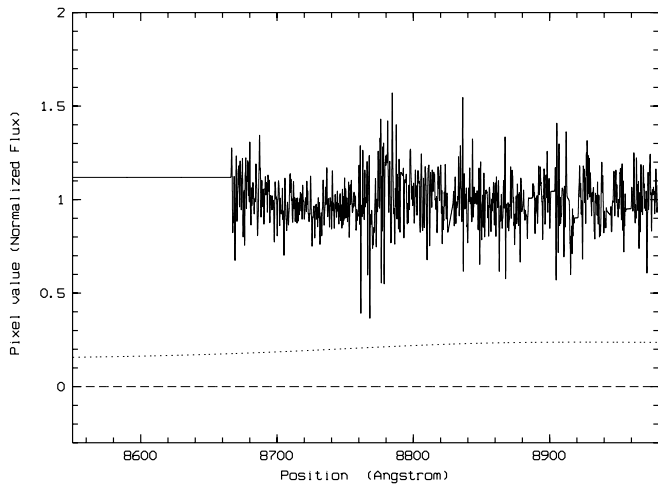
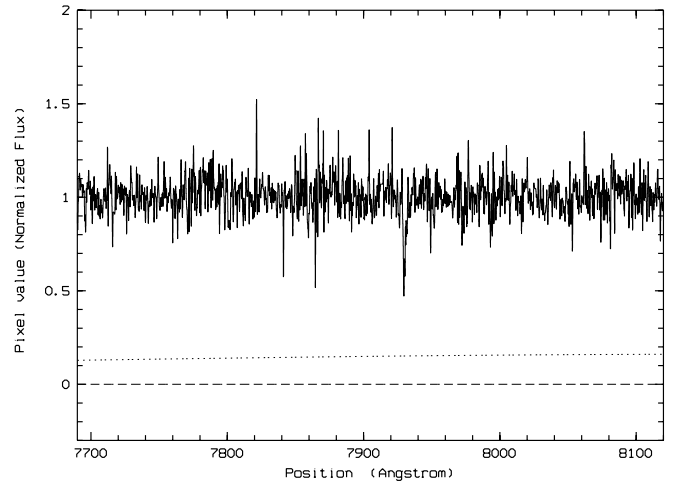
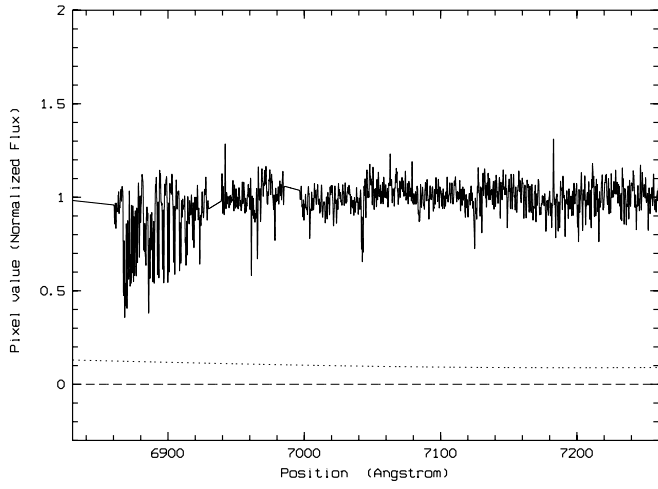


FIG. 1.—Continued

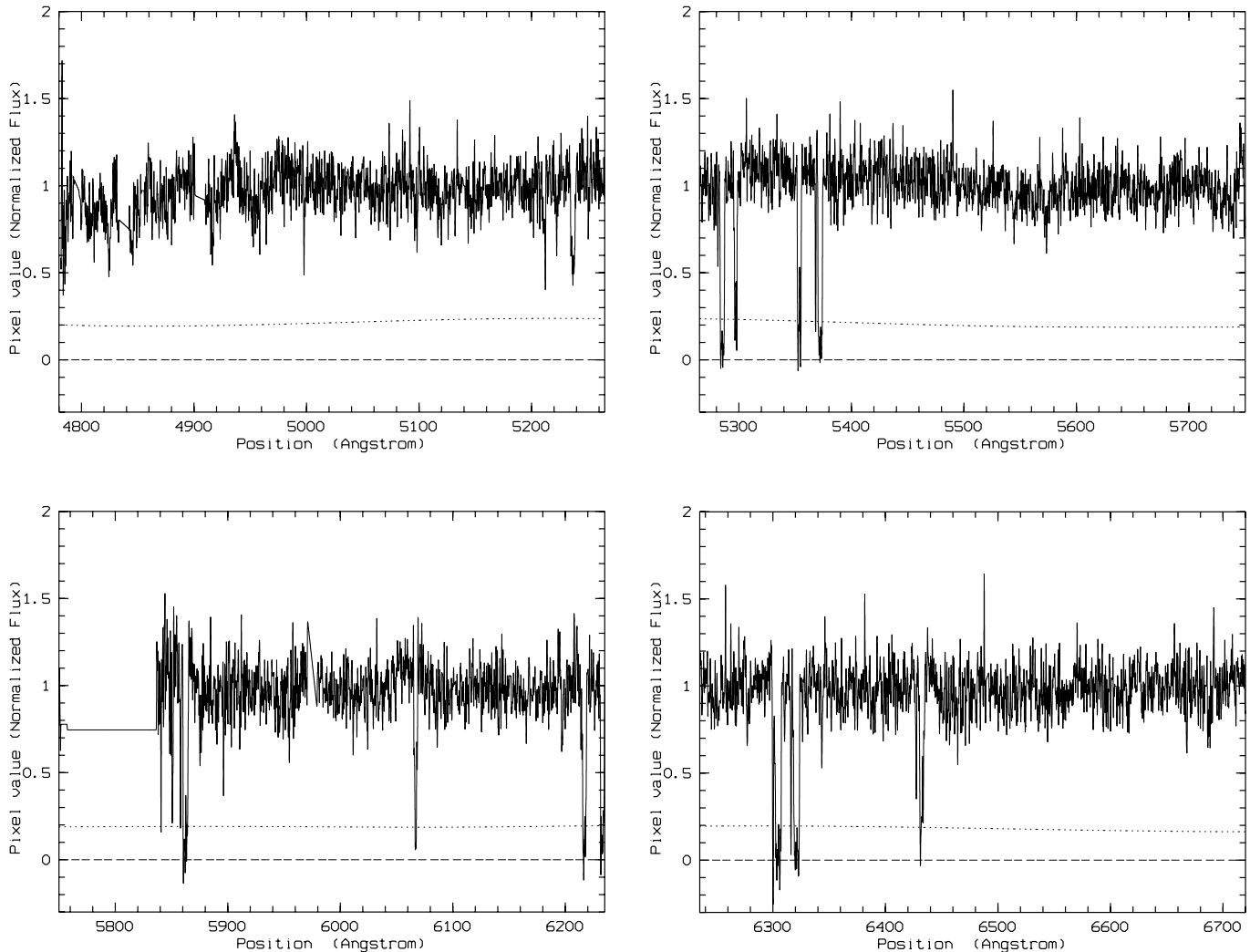


FIG. 2.—Same as Fig. 1, but for GRB 020813.

to  $\sim 9400$  Å and were rebinned to  $0.1$  Å to increase the signal-to-noise ratio. The resulting resolution element, set to 2 pixels, ranges then from  $14 \text{ km s}^{-1}$  at  $4200$  Å to  $6.6 \text{ km s}^{-1}$  at  $9000$  Å. The noise spectrum, used to determine the errors on the best-fit line parameters, has been calculated from the real background-subtracted and rebinned spectrum using line-free regions. This therefore takes into account both statistical errors and systematic errors in the pipeline processing and background subtraction. Table 2 gives the signal-to-noise ratio per  $0.1$  Å pixel at different wavelengths for the four spectra in Table 1. Figure 1 plots the full UVES spectrum of GRB 021004, for which both UVES dichroics, and both red and blue arms, were used, allowing us to obtain a particularly wide spectral coverage, extending from  $\sim 4250$  to  $\sim 9400$  Å. A further dichroic 1, blue arm image covering the band  $3400$ – $3900$  Å was obtained, but the signal-to-noise ratio is too low to allow a reliable extraction of the spectrum in this band. Figure 2 plots the full UVES spectrum of GRB 020813. This spectrum, as well as the spectrum in Figure 1, was smoothed with a Gaussian function with  $\sigma = 1.5$  pixels. Tables 3 and 4 give the equivalent width of all lines detected in the UVES spectra for the two GRB afterglows, along with their identification. The equivalent widths are computed at the redshift of the absorption systems. For the GRB host galaxy-identified systems and the two main intervening systems at  $z = 1.60$  and  $1.38$  we also report faint lines with signal-to-noise

ratio  $>1$ . Unidentified lines are reported only if the signal-to-noise ratio is  $>3$ . Their equivalent widths are computed at zero redshift.

### 3. COLUMN DENSITIES

In this paper we focus on the systems that are likely to be associated with the GRB host galaxies. The line fitting was performed using the MIDAS package FITLYMAN (Fontana & Ballester 1995). This uses a Voigt profile and independently yields the column density  $N$  and the Doppler parameter  $b$  for each absorption component. For each absorption system several lines, spread over the entire spectral range covered by the UVES observations, were fitted simultaneously, using the same number of components for each line and the same redshift and  $b$ -value for each component.

#### 3.1. GRB 021004

For this GRB we consider the absorption systems at the following redshifts and velocities (in  $\text{km s}^{-1}$ ) with respect to the Ly $\alpha$  emission of the host galaxy (Mirabal et al. 2003):  $z = 2.328$ ,  $v = 0$  (system A in Fig. 3);  $z = 2.328$ ,  $v = -139 \text{ km s}^{-1}$  (system B);  $z = 2.328$ ,  $v = -224 \text{ km s}^{-1}$  (system C);  $z = 2.321$ ;  $z = 2.298$ ; and  $z = 2.296$ . For these systems we detected C IV, C II, Si IV, Al II, Al III, Mg II, and Fe II lines (see Table 3). In the table we also report the tentative identification of an

TABLE 3  
GRB 021004 UVES LINE IDENTIFICATIONS

$\lambda$ (Å)	$W_{\text{rest}}^a$ (Å)	ID	$z$
4298.40.....	0.13 ± 0.02	?Si II $\lambda$ 1304.37?	?2.2953?
4301.73.....	0.06 ± 0.03	Si II $\lambda$ 1808.01	1.3793–8
4304.53.....	0.09 ± 0.03	Si II $\lambda$ 1808.01	1.3807
4311.20.....	0.16 ± 0.08	...	...
4346.30.....	0.27 ± 0.08	Al II $\lambda$ 1670.79	1.6014
4347.25.....	0.18 ± 0.03	Al II $\lambda$ 1670.79	1.6019
4348.60.....	0.11 ± 0.03	Al II $\lambda$ 1670.79	1.6028
4350.95.....	0.53 ± 0.08	...	...
4358.28.....	0.35 ± 0.08	...	...
4398.34.....	0.06 ± 0.03	C II $\lambda$ 1334.53	2.2958
4401.68.....	0.24 ± 0.02	C II $\lambda$ 1334.53	2.2981–4+
4415.50.....	0.10 ± 0.03	?C II* $\lambda$ 1335.70?	?2.2958?
4441.34.....	0.04 ± 0.02	Al III $\lambda$ 1854.71	1.3807
4445.35.....	0.09 ± 0.02	C II $\lambda$ 1334.53	2.328
4455.35.....	0.09 ± 0.02	C II* $\lambda$ 1335.70	2.328
4593.59.....	0.15 ± 0.02	Si IV $\lambda$ 1393.76	2.2958
4596.71.....	0.02 ± 0.02	Si IV $\lambda$ 1393.76	2.2981–4
4623.48.....	0.21 ± 0.02	Si IV $\lambda$ 1402.77	2.2958
4626.41.....	0.02 ± 0.02	Si IV $\lambda$ 1402.77	2.2981–4
4629.72.....	0.40 ± 0.02	Si IV $\lambda$ 1393.76	2.321
4631.35.....	0.30 ± 0.07	...	...
4635.85.....	0.65 ± 0.07	...	...
4637.38.....	3.63 ± 0.07	...	...
4638.01.....	0.31 ± 0.02	Si IV $\lambda$ 1393.76	2.328
4643.19.....	0.25 ± 0.07	...	...
4658.07.....	0.27 ± 0.02	Si IV $\lambda$ 1402.77	2.321
4666.28.....	1.07 ± 0.07	...	...
4668.38.....	0.56 ± 0.02	Si IV $\lambda$ 1393.76	2.328
5102.54.....	0.50 ± 0.02	C IV $\lambda$ 1548.20	2.2958
5106.50.....	0.35 ± 0.02	C IV $\lambda$ 1548.20	2.2981–4
5111.04.....	0.33 ± 0.02	C IV $\lambda$ 1550.77	2.2958
5114.82.....	0.16 ± 0.02	C IV $\lambda$ 1550.77	2.2981–4
5141.11.....	1.74 ± 0.02	C IV $\lambda$ 1448.20	2.321
5150.4.....	2.10 ± 0.02	C IV $\lambda$ 1550.77	2.321+
5159.66.....	1.57 ± 0.02	C IV $\lambda$ 1448.20	2.328
5159.66.....	1.57 ± 0.02	C IV $\lambda$ 1550.77	2.328
5510.62.....	0.05 ± 0.02	Al II $\lambda$ 1670.79	2.2981–4
5560.30.....	0.47 ± 0.02	Al II $\lambda$ 1670.79	2.328
5577.71.....	1.47 ± 0.03	Fe II $\lambda$ 2344.21	1.3793–8
5580.81.....	0.07 ± 0.03	Fe II $\lambda$ 2344.21	1.3807
5592.94.....	0.14 ± 0.06	...	...
5649.59.....	0.31 ± 0.03	Fe II $\lambda$ 2374.21	1.3793–8
5669.68.....	0.67 ± 0.03	Fe II $\lambda$ 2382.77	1.3793–8
6064.56.....	0.60 ± 0.06	...	...
6098.32.....	0.22 ± 0.06	...	...
6099.33.....	0.19 ± 0.02	Fe II $\lambda$ 2344.21	1.6019
6101.32.....	0.09 ± 0.02	Fe II $\lambda$ 2344.21	1.6028
6154.64.....	0.52 ± 0.03	Fe II $\lambda$ 2586.65	1.3793–8
6158.03.....	0.01 ± 0.03	Fe II $\lambda$ 2586.65	1.3807
6160.76.....	0.17 ± 0.06	...	...
6172.42.....	0.35 ± 0.02	Al III $\lambda$ 1854.72	2.328
6176.74.....	0.21 ± 0.06	...	...
6177.88.....	0.17 ± 0.02	Fe II $\lambda$ 2374.46	1.6019
6180.04.....	0.14 ± 0.05	...	...
6186.51.....	0.25 ± 0.02	Al III $\lambda$ 1862.79	2.321+
6186.99.....	0.11 ± 0.02	Fe II $\lambda$ 2600.17	1.3793–8
6187.81.....	0.05 ± 0.02	Fe II $\lambda$ 2600.17	1.3798
6190.23.....	0.12 ± 0.02	Fe II $\lambda$ 2600.17	1.3807
6199.36.....	0.11 ± 0.02	Al III $\lambda$ 1862.79	2.328+
6198.4.....	...	...	...
6199.53.....	0.29 ± 0.02	Fe II $\lambda$ 2382.77	1.6019
6201.66.....	0.28 ± 0.02	Fe II $\lambda$ 2382.77	1.6028
6653.88.....	0.89 ± 0.02	Mg II $\lambda$ 2796.35	1.3793–8
6655.88.....	0.24 ± 0.02	Mg II $\lambda$ 2796.35	1.3802

TABLE 3—Continued

$\lambda$ (Å)	$W_{\text{rest}}^a$ (Å)	ID	$z$
6657.60.....	0.47 ± 0.02	Mg II $\lambda$ 2796.35	1.3807
6671.00.....	0.78 ± 0.02	Mg II $\lambda$ 2803.53	1.3793–8
6672.73.....	0.06 ± 0.02	Mg II $\lambda$ 2803.53	1.3802
6674.77.....	0.32 ± 0.02	Mg II $\lambda$ 2803.53	1.3807
6730.16.....	0.25 ± 0.02	Fe II $\lambda$ 2586.65	1.6019
6732.55.....	0.09 ± 0.02	Fe II $\lambda$ 2586.65	1.6028
6750.64.....	0.08 ± 0.02	Mn II $\lambda$ 2594.50	1.6019
6764.18.....	0.43 ± 0.04	...	...
6765.43.....	0.25 ± 0.02	Fe II $\lambda$ 2600.17	1.6019
6767.79.....	0.17 ± 0.02	Fe II $\lambda$ 2600.17	1.6028
6768.78.....	0.18 ± 0.04	...	...
6781.81.....	0.04 ± 0.02	Mn II $\lambda$ 2606.46	1.6019
6788.06.....	0.03 ± 0.02	Mg I $\lambda$ 2852.94	1.3793–8
7003.91.....	0.12 ± 0.03	...	...
7041.91.....	0.12 ± 0.03	...	...
7042.52.....	0.11 ± 0.03	...	...
7043.25.....	0.10 ± 0.03	...	...
7274.52.....	0.26 ± 0.01	Mg II $\lambda$ 2796.35	1.6014
7275.83.....	0.33 ± 0.01	Mg II $\lambda$ 2796.35	1.6019
7277.28.....	0.49 ± 0.01	Mg II $\lambda$ 2796.35	1.6024
7278.39.....	0.24 ± 0.01	Mg II $\lambda$ 2796.35	1.6028
7293.12.....	0.27 ± 0.01	Mg II $\lambda$ 2803.53	1.6014
7294.58.....	0.36 ± 0.01	Mg II $\lambda$ 2803.53	1.6019
7295.91.....	0.04 ± 0.01	Mg II $\lambda$ 2803.53	1.6024
7296.85.....	0.23 ± 0.01	Mg II $\lambda$ 2803.53	1.6028
7422.05.....	0.04 ± 0.01	Mg I $\lambda$ 2852.94	1.6014
7423.01.....	0.23 ± 0.01	Mg I $\lambda$ 2852.94	1.6019
7929.74.....	0.75 ± 0.05	...	...
7929.53.....	0.08 ± 0.02	Fe II $\lambda$ 2382.77	2.328
7930.42.....	0.04 ± 0.02	Fe II $\lambda$ 2382.77	2.328
7931.03.....	0.03 ± 0.02	Fe II $\lambda$ 2382.77	2.328
8228.16.....	0.37 ± 0.05	...	...
9178.45.....	0.75 ± 0.08	...	...
9205.45.....	0.70 ± 0.09	...	...
9216.41.....	0.04 ± 0.03	Mg II $\lambda$ 2796.35	2.2958
9222.70.....	0.09 ± 0.03	Mg II $\lambda$ 2796.35	2.2981
9223.62.....	0.18 ± 0.03	Mg II $\lambda$ 2796.35	2.2984
9246.33.....	0.09 ± 0.03	Mg II $\lambda$ 2803.53	2.2981
9247.39.....	0.12 ± 0.03	Mg II $\lambda$ 2803.53	2.2984
9330.33.....	0.57 ± 0.03	Mg II $\lambda$ 2803.53	2.328

NOTES.—Question marks indicate uncertain identification. In many cases several components contribute to a single line in one entry of the table. In these cases either the redshift is given with only four digits or it is given as a range. A plus sign indicates that a line is partly blended with the following entry.

<sup>a</sup> The equivalent width of unidentified lines is computed at zero redshift.

Si II  $\lambda$ 1304 line at  $z = 2.2953$ . This is close but not coincident with the redshift of systems  $z = 2.296$ . We therefore consider this identification uncertain, and we do not consider this line in the following analysis.

Unfortunately, the Ly $\alpha$  absorption associated with the  $z = 2.328$  systems falls exactly in the gap between the dichroic 1 and 2 blue arm spectra and therefore is not covered in this study. Zn II and Cr II absorption lines for the main  $z = 2.328$  and 2.321 systems fall in the region affected by atmospheric telluric features (see Fig. 1) and are therefore not accessible.

Figure 3 shows the C IV and Si IV doublets of the above six systems. Note that the C IV  $\lambda$ 1548 lines of the  $z = 2.328$  A, B, C systems are strongly blended with the C IV  $\lambda$ 1550 line of the  $z = 2.321$  system, while the Si IV  $\lambda$ 1404 line of the  $z = 2.298$  system is blended with the Si IV  $\lambda$ 1393 line of the  $z = 2.321$  system. Each of the six systems actually comprises several

TABLE 4  
GRB 020813 UVES LINE IDENTIFICATIONS

$\lambda$ (Å)	$W_{\text{rest}}^a$ (Å)	ID	$z$
4824.64.....	1.06 ± 0.05	...	...
4824.64.....	0.59 ± 0.05	...	...
4998.03.....	0.47 ± 0.05	...	...
5212.23.....	0.18 ± 0.03	Fe II $\lambda$ 2344.21	1.2234
5236.74.....	1.64 ± 0.07	...	...
5281.33.....	0.09 ± 0.03	Fe II $\lambda$ 2344.21	1.2529
5285.19.....	1.70 ± 0.03	Fe II $\lambda$ 2344.21	1.255
5297.11.....	0.85 ± 0.03	Fe II $\lambda$ 2382.77	1.2234
5353.61.....	1.31 ± 0.03	Fe II $\lambda$ 2374.46	1.255
5368.21.....	0.28 ± 0.03	Fe II $\lambda$ 2382.77	1.2529
5372.23.....	1.63 ± 0.03	Fe II $\lambda$ 2382.77	1.255
5840.73.....	0.44 ± 0.06	...	...
5850.86.....	0.73 ± 0.06	...	...
5858.24.....	0.23 ± 0.02	Fe II $\lambda$ 2600.17	1.2529
5862.33.....	1.82 ± 0.02	Fe II $\lambda$ 2600.17	1.255
5896.25.....	0.40 ± 0.06	...	...
6067.05.....	2.30 ± 0.06	...	...
6216.93.....	1.34 ± 0.03	Mg II $\lambda$ 2796.35	1.2234
6232.85.....	1.36 ± 0.03	Mg II $\lambda$ 2803.53	1.2234
6300.13.....	0.55 ± 0.03	Mg II $\lambda$ 2796.35	1.2529
6304.72.....	2.38 ± 0.03	Mg II $\lambda$ 2796.35	1.255
6310.38.....	0.30 ± 0.06	...	...
6316.13.....	0.30 ± 0.03	Mg II $\lambda$ 2803.53	1.2529
6321.11.....	2.19 ± 0.03	Mg II $\lambda$ 2803.53	1.255
6343.49.....	0.11 ± 0.03	Mg I $\lambda$ 2852.13	1.2234
6427.36.....	0.24 ± 0.03	Mg I $\lambda$ 2852.13	1.2529
6432.12.....	1.34 ± 0.03	Mg I $\lambda$ 2852.13	1.255
6686.87.....	0.27 ± 0.03	Fe I $\lambda$ 2967.76	1.2529

NOTE.—Errors are 67% confidence intervals.

<sup>a</sup> The equivalent width of unidentified lines is computed at zero redshift.

components, within a velocity range of several tens of kilometers per second. For this reason the identification of the different systems is somewhat subjective, the true message being that the geometry and kinematics of the ISM clouds probed by the GRB line of sight are complex. Nevertheless, sticking to the above system identifications will be useful.

There are 13 lines in Table 3 associated with the  $z = 2.328$  systems, five lines associated with the  $z = 2.321$  system, and up to 17 lines associated to the  $z = 2.296$ – $2.298$  systems. Some of these lines can be split further into several components. To test the robustness of the fit, in terms of the accuracy and stability of the results, we performed many fits, using several combinations of lines/systems. We found that the fits presented below are a good compromise between increasing the statistical precision of the fit, obtained by increasing the number of lines fitted simultaneously, and the stability/repeatability of the results, which degraded when the number of fitted parameters was increased, because of the increasingly complex shape of the  $\chi^2$  hypersurface in the parameter space, which may contain many local minima.

For the  $z = 2.328$  A, B, C and  $z = 2.321$  systems we simultaneously fitted the C IV  $\lambda\lambda$ 1550, 1548, C II  $\lambda$ 1334, C II\*  $\lambda$ 1335, Si IV  $\lambda\lambda$ 1404, 1393, Al II  $\lambda$ 1670, and the Al III  $\lambda$ 1854 lines. We excluded from the fit the  $z = 2.328$  Al III  $\lambda$ 1862 line because its blue wing is strongly blended with another line and the  $z = 2.321$  Al III  $\lambda$ 1862 line because it is strongly blended with the Fe II  $\lambda$ 2600 line of one of the components of the  $z = 1.38$  intervening system. For the same systems we also fitted the Fe II  $\lambda$ 2382, Fe II  $\lambda$ 2374, Fe II  $\lambda$ 2344, Fe II  $\lambda$ 1608, Mg II  $\lambda$ 2803, and Mg II  $\lambda$ 2796 lines simultaneously. Figure 4 shows the line spectra in velocity

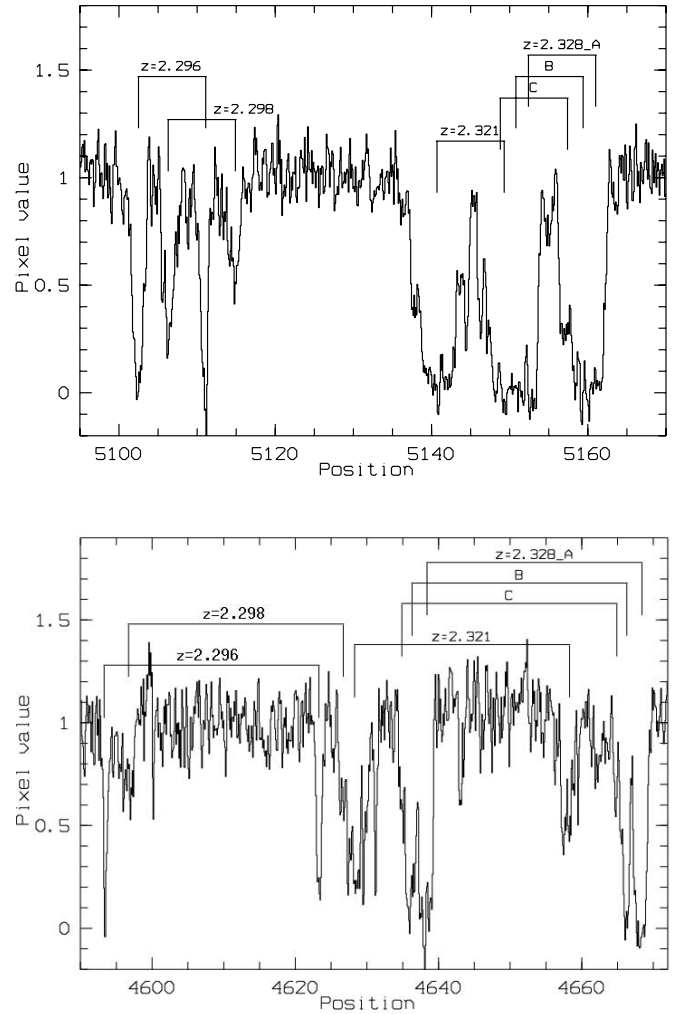


FIG. 3.—C IV (top) and Si IV (bottom) absorption systems in the UVES spectra of GRB 021004 for  $z = 2.328$  (see Table 5).

space, along with the best-fit model, while Table 5 presents the best-fit abundances along with the velocity shift of each system with respect to the redshift of the host galaxy, assumed to be 2.328 for GRB 021004 (Mirabal et al. 2003). We used two components for the  $z = 2.328$  A system and one component for the other three systems. The best-fit Doppler parameter  $b$  ranges from a minimum of  $12 \pm 6$  km s<sup>-1</sup> (one of the components of the  $z = 2.328$  A system) up to a maximum of  $107 \pm 10$  km s<sup>-1</sup> (system  $z = 2.321$ ). Of course, different  $b$ -values are obtained using a higher (or lower) number of components. Unfortunately, the signal-to-noise ratio of our spectrum is not good enough to unambiguously identify the different components. On the other hand, we verified that the total best-fit column density of each system is stable, within the statistical errors, to changing the number of components in each system.

Similar series of fits were performed for the  $z = 2.296$  and  $2.298$  systems, for which we used one and two components, respectively (see Fig. 5). Table 5 again gives the best-fit abundances for these two systems. The best-fit Doppler parameter  $b$  ranges from  $9 \pm 7$  to  $40 \pm 13$  km s<sup>-1</sup>.

The detection of both high- and low-ionization lines, feasible thanks to the extremely wide spectral coverage achieved by UVES, allows us to obtain constraints on the ionization status of the gas responsible for the UV absorption, by comparing ion column density ratios with the predictions of photoionization codes.

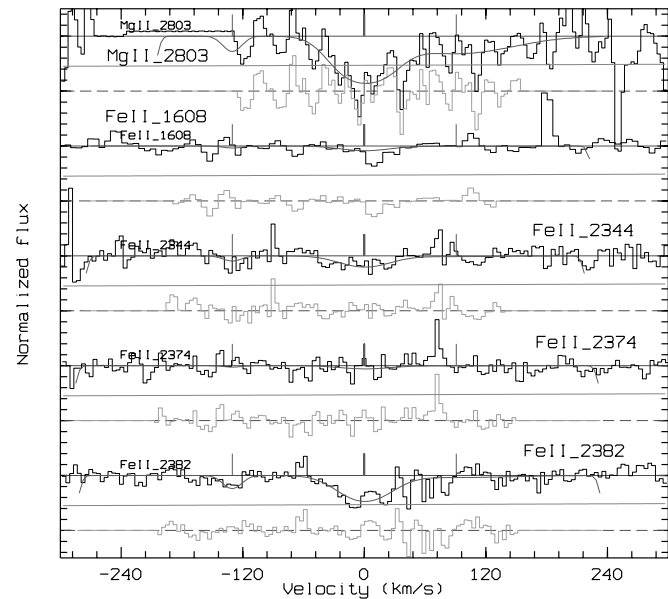
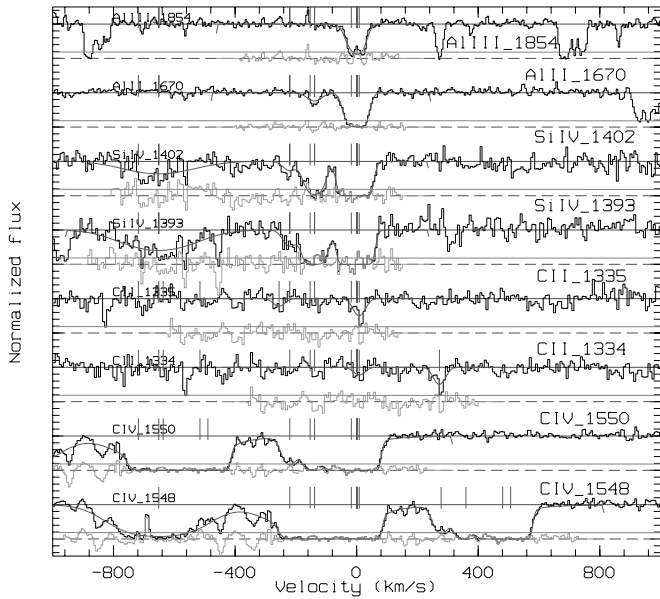


FIG. 4.—GRB 021004. *Top*: UVES spectrum near the C IV  $\lambda\lambda 1550, 1548$ , C II  $\lambda 1334$ , C II\*  $\lambda 1335$ , Si IV  $\lambda\lambda 1404, 1393$ , Al II  $\lambda 1670$ , and Al III  $\lambda 1854$  lines for the  $z = 2.328$  and  $2.321$  systems in velocity space, along with the best-fit model (*solid line*) and residuals (*gray line*). *Bottom*: Same for the Fe II  $\lambda 2382$ , Fe II  $\lambda 2374$ , Fe II  $\lambda 2344$ , Fe II  $\lambda 1608$ , and Mg II  $\lambda 2803$  lines. The zero in the velocity scale refers to the redshift of the host galaxy. [See the electronic edition of the *Journal* for a color version of this figure.]

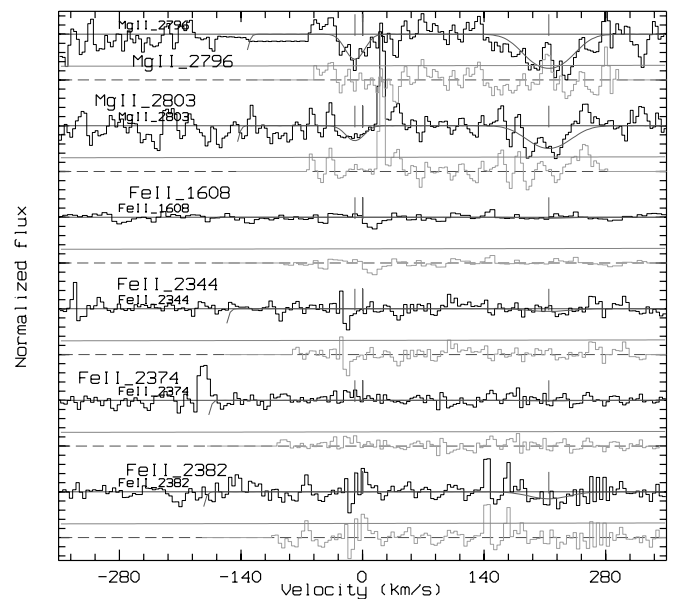
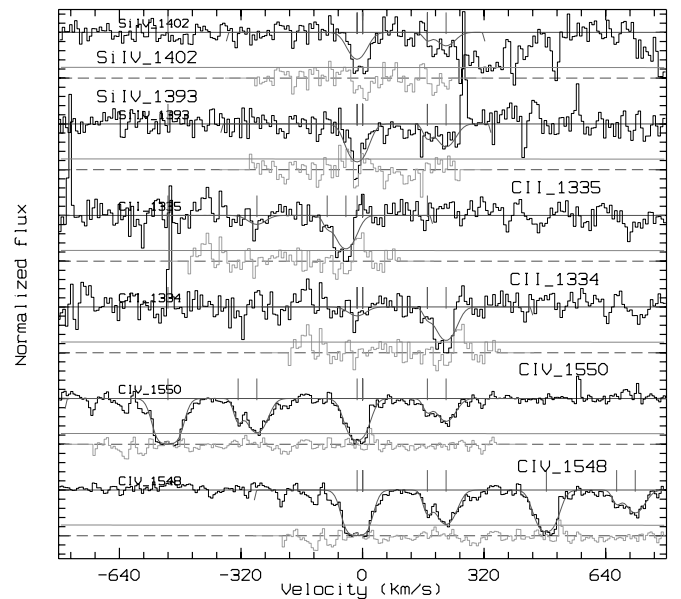


FIG. 5.—GRB 021004. *Top*: UVES spectrum near the C IV  $\lambda\lambda 1550, 1548$ , C II  $\lambda 1334$ , C II\*  $\lambda 1335$ , and Si IV  $\lambda\lambda 1404, 1393$  lines for the  $z = 2.298$  and  $2.296$  systems in velocity space, along with the best-fit model (*solid line*) and residuals (*gray line*). *Bottom*: Same for the Fe II  $\lambda 2382$ , Fe II  $\lambda 2374$ , Fe II  $\lambda 2344$ , Fe II  $\lambda 1608$ , Mg II  $\lambda 2803$ , and Mg II  $\lambda 2796$  lines. The zero in the velocity scale refers to  $z = 2.296$ . [See the electronic edition of the *Journal* for a color version of this figure.]

TABLE 5  
GRB 021004 LOGARITHMIC ION COLUMN DENSITIES

System	Velocity Shift (km s <sup>-1</sup> )	Si IV (cm <sup>-2</sup> )	C IV (cm <sup>-2</sup> )	C II (cm <sup>-2</sup> )	C II* (cm <sup>-2</sup> )	Al II (cm <sup>-2</sup> )	Fe II (cm <sup>-2</sup> )	Mg II (cm <sup>-2</sup> )
2.328 A .....	0	15.30 ± 0.56	>15.2	13.40 ± 0.45	13.90 ± 0.58	13.55 ± 0.35 <sup>a</sup>	13.34 ± 0.15	13.82 ± 0.24
2.328 B .....	-139	14.27 ± 0.16	>14.4	<13.2	<13.2	12.23 ± 0.35	12.53 ± 0.24	12.93 ± 0.60
2.328 C .....	-224	13.24 ± 0.17	14.40 ± 0.11	<13.2	<13.2	<12.0	<12.3	<12.8
2.321.....	-632	14.11 ± 0.08	15.04 ± 0.05	<13.2	<13.2	<12.0	<12.3	<12.8
2.298.....	-2729	13.43 ± 0.33	14.16 ± 0.20	14.28 ± 0.20 <sup>b</sup>	<13.2	<12.0	12.68 ± 0.20	13.22 ± 0.10
2.296.....	-2913	13.79 ± 0.16	14.72 ± 0.25	13.43 ± 0.40	<sup>b</sup>	<12.0	<12.3	12.68 ± 0.21

NOTE.—Errors, upper and lower limits are 90% confidence intervals.

<sup>a</sup> For system  $z = 2.328$  A we also measured a column density of Al III of  $13.66 \pm 0.30$ .

<sup>b</sup> The  $z = 2.296$  C II\* line is completely blended with the  $z = 2.298$  C II line.

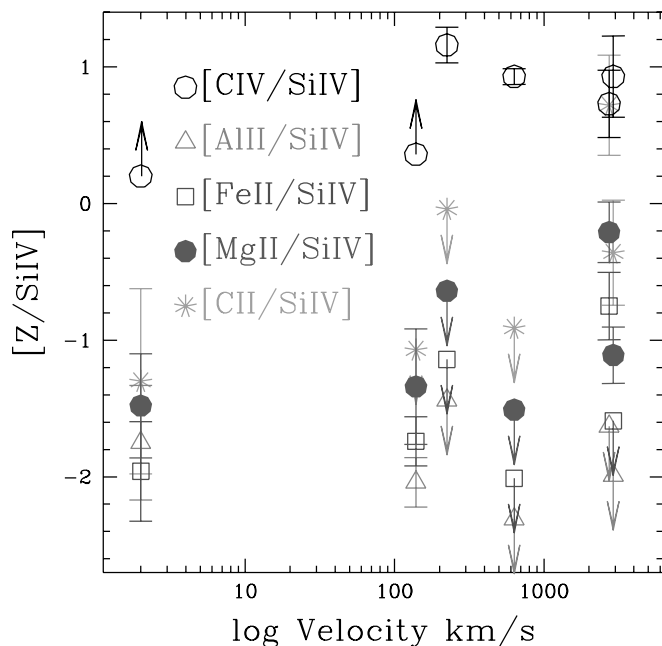


FIG. 6.—Logarithmic ratio of the C IV, C II, Fe II, Al II, and Mg II column densities to that of Si IV for the six absorption systems as a function of the negative velocity shift with respect to the redshift of the host galaxy. [See the electronic edition of the *Journal* for a color version of this figure.]

Unfortunately, we were not able to measure column densities of different ions of the same element, except for C II/C IV and Al II/Al III for system  $z = 2.328$  A and C II/C IV for system  $z = 2.298$ . In the other cases we are forced to use ratios of column densities of different ions of different elements in this analysis. These estimates of the gas ionization parameter are therefore somewhat degenerate with respect to relative element abundances. We used the Grevesse & Anders (1989) meteoritic abundances with extensions by Grevesse et al. (1993).

Figure 6 shows the logarithmic ratio between the C IV, C II, Fe II, Al II, and Mg II column densities and that of Si IV for the six absorption systems as a function of the velocity shift with respect to the redshift of the host galaxy. No large variation of the ion ratios is seen for the six systems. We compared these line ratios to the predictions obtained by simulating a gas cloud illuminated by an ionizing continuum. We used CLOUDY (ver. 90.04; Ferland 2002) to build grids of photoionization models as a function of  $U$ , the ionization parameter.  $U$  is defined as the ratio between the ionizing photon density and the electron density of the gas. It is computed assuming a constant density profile throughout the cloud and a plane-parallel geometry. We studied gas densities between 1 and  $10^8$   $\text{cm}^{-3}$ . The ionizing continuum was assumed to be a power law,  $F(E) = E^{-\Gamma}$  photons  $\text{cm}^{-2} \text{s}^{-1}$ , with cutoffs at low and high energies. The high-energy cutoff is fixed at  $10^{21}$  Hz, while we run the simulations for different low-energy cutoffs, from  $10^{10}$  to  $10^{14}$  Hz. We produced several sets of simulations with  $\Gamma$  in the range 1–2. The ionizing continuum is constant in time. GRBs are highly variable sources, and the ionization structure of the gas can be better studied using a time-dependent photoionization code, such as those of Nicastro et al. (1999) and Perna & Lazzati (2002). Nevertheless, our simpler approach is instructive in identifying general trends.

The predicted photoionization equilibrium ion ratios of [Mg II/Si IV], [Fe II/Si IV], [Al II/Si IV], and [C IV/Si IV] are shown in Figure 7 for  $\Gamma = 2$  and  $n = 1$   $\text{cm}^{-3}$  and Figure 8 for  $\Gamma = 2$  and  $n = 10^8$   $\text{cm}^{-3}$ . For each of the six redshift systems, thick

segments superposed on these curves indicate our 90% confidence determinations for these ratios. In Figure 7 (for  $n = 1$   $\text{cm}^{-3}$ ) the [Mg II/Si IV], [Fe II/Si IV], and [Al II/Si IV] ion ratios for the systems  $z = 2.328$  A,  $z = 2.328$  B,  $z = 2.328$  C, and  $z = 2.296$  are all consistent with the same ionization status. For the system  $z = 2.328$  A we measured the column density of Al II and Al III. Their ratio is also consistent with the ionization parameter inferred from the above ion ratios (see Figs. 7 and 8). For the same system we measured the column density of C II. The [C II/Si IV] ion ratio indicates an ionization parameter somewhat higher than that indicated by the other ion ratios for  $n = 1$   $\text{cm}^{-3}$  (see Fig. 7), while for  $n = 10^8$   $\text{cm}^{-3}$  the ionization parameter is fully consistent with that indicated by the other ion ratios (Fig. 8). The system at  $z = 2.298$  shows an ionization parameter lower than that of system  $z = 2.328$  A, while the system at  $z = 2.321$  shows a higher ionization parameter. However, all ionization parameter systems are consistent with a remarkably narrow range:  $10^{-1.7} < U < 10^{-1}$  for  $n = 1$   $\text{cm}^{-3}$  and  $10^{-1.2} < U < 10^{-1}$  for  $n = 10^8$   $\text{cm}^{-3}$ ; see Figure 9, which plots the ionization parameters as a function of the velocity for the six systems. We note that in these ranges of  $U$  the [Fe II/Mg II] ratio varies by less than 30%, and the value found for the three systems in which we detect Fe II and Mg II lines ([Mg II/Fe II]  $\approx 0.4$ ) is consistent with what is expected from meteoritic abundances (and as was adopted for the CLOUDY calculations). This value is also in the range found for the Galactic ISM,  $0.1 < [\text{Mg}/\text{Fe}] < 0.8$ . It is somewhat higher than that found by Savaglio et al. (2004) in a sample of faint  $K$ -band-selected galaxies at  $1.4 < z < 2.0$ ,  $-0.84 < [\text{Mg}/\text{Fe}] < 0.13$ . Assuming meteoritic abundances, the hydrogen column density of the densest system ( $z = 2.328$  A) is  $\gtrsim 5 \times 10^{19}$   $\text{cm}^{-2}$ , where the equality yields if all Si is in the form of Si IV. This column is so low that it would have easily escaped detection in the *Chandra* X-ray spectrum (Butler et al. 2003), and it is consistent with the upper limit given by Møller et al. (2003).

Qualitatively similar results are drawn from the analysis of the  $n = 10^8$   $\text{cm}^{-3}$  curves, although the range of acceptable ionization parameters for the six systems is narrower (see Fig. 8). Qualitatively similar results were also obtained for the  $\Gamma = 1$  models.

### 3.1.1. The $z = 2.328$ A System

For this system we detect the C II\*  $\lambda 1335$  fine-structure line. Unfortunately, the C II  $\lambda 1334$  ground-state line is barely visible (with a signal-to-noise ratio of just 2). The presence of a strong C II\* line suggests either a high gas density or a strong radiation field (Srianand & Petitjean 2000, 2001; Silva & Viegas 2002). C II\* and Si II\* fine-structure lines have been detected in two other GRBs: GRB 020813 (Savaglio & Fall 2004) and GRB 030323 (Vreeswijk et al. 2004). Their ratio can be used to constrain the gas density or the radiation field (if both lines are detected, one may solve for both variables, as shown by Srianand & Petitjean 2000), so their detection in GRB spectra looks very promising for constraining the physical properties of the absorbing gas.

For this system the C IV line is strongly saturated, so it cannot be used together with the C II to constrain the gas ionization status. As discussed in the previous section, within rather large uncertainties, the [C II/Si II] would suggest for  $n = 1$   $\text{cm}^{-3}$  an ionization parameter somewhat higher than that indicated by all other line ratios, assuming meteoritic abundances. This may be explained by a slight underabundance of C with respect to Si in this system. A similar conclusion applies to system  $z = 2.321$ ; see below.

The C IV  $\lambda 1548$  lines of the  $z = 2.328$  A, B, and C systems are blended with the C IV  $\lambda 1550$  of the  $z = 2.321$  system, suggesting

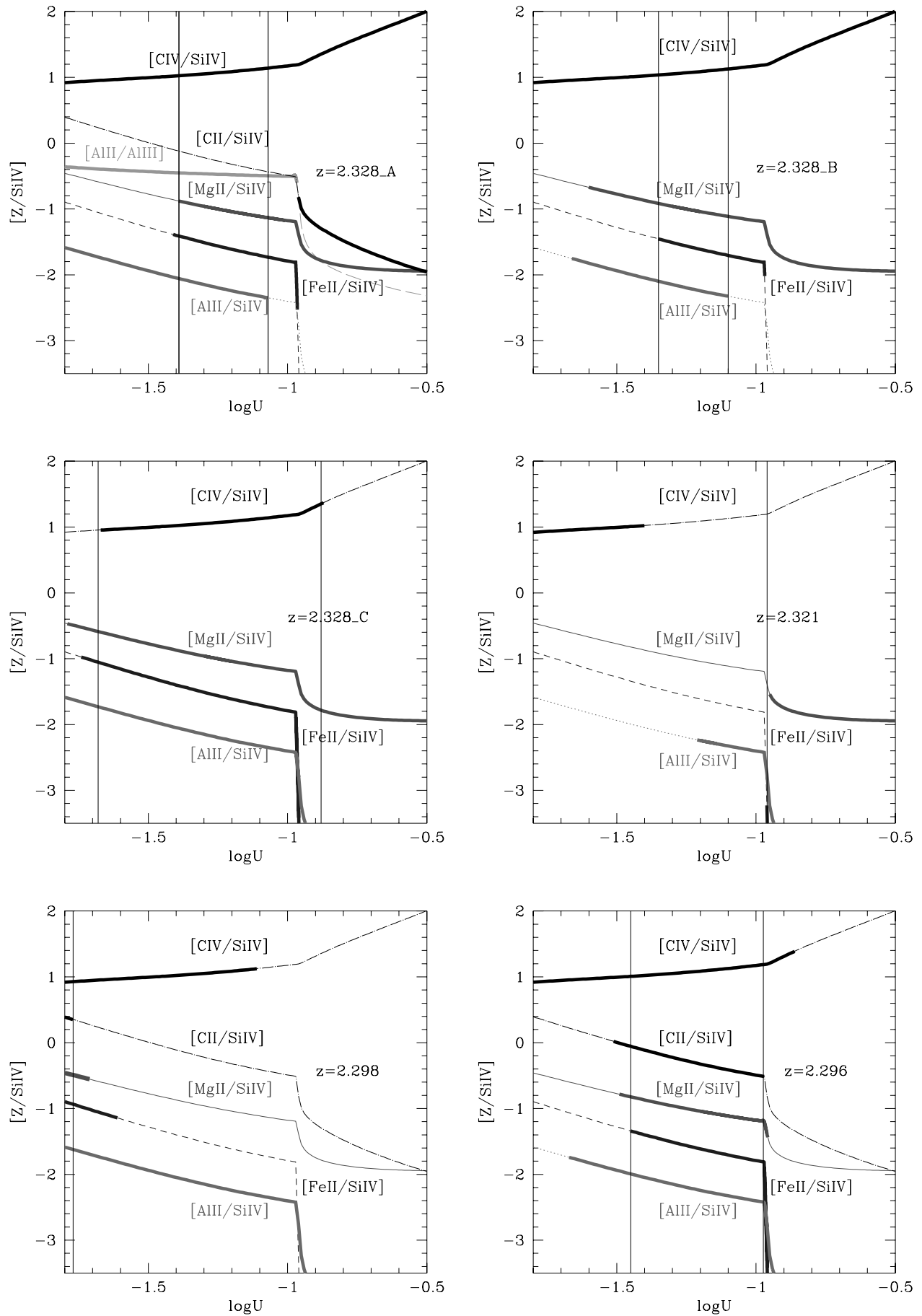


FIG. 7.—Ion ratios from CLOUDY models for the six absorption systems, assuming a gas density of  $1 \text{ cm}^{-3}$ :  $[Mg \text{ II}/Si \text{ IV}]$  (solid curves),  $[Fe \text{ II}/Si \text{ IV}]$  (dashed curves),  $[Al \text{ II}/Si \text{ IV}]$  (dotted curves), and  $[C \text{ IV}/Si \text{ IV}]$  and  $[C \text{ II}/Si \text{ IV}]$  (dot-dashed black curves). The line indicating the model values is thick when it is consistent within 90% with the measured ion ratios. The vertical solid lines mark the range of allowed  $U$  values in each panel. [See the electronic edition of the Journal for a color version of this figure.]

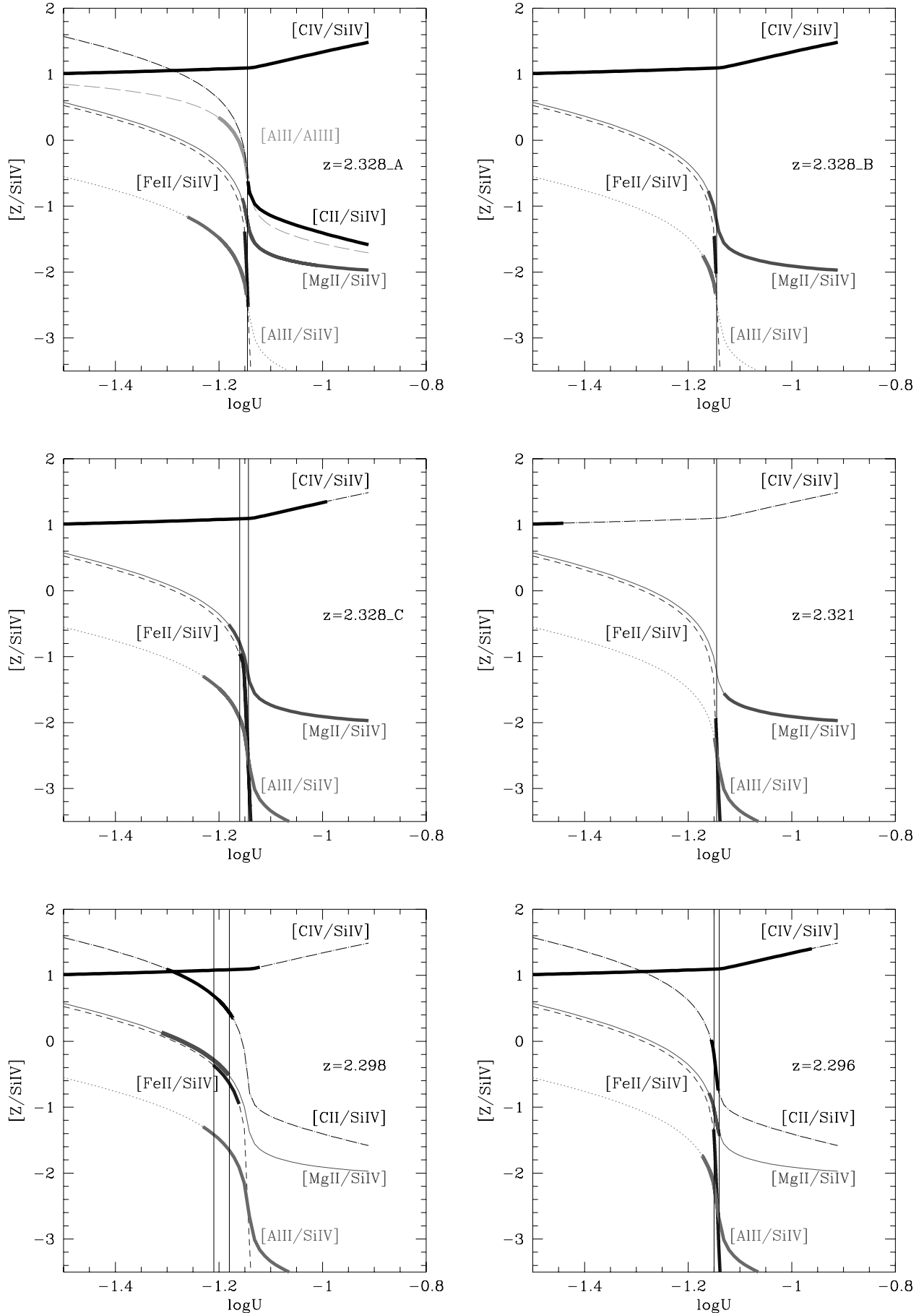


FIG. 8.—Ion ratios from CLOUDY photoionization models for the six absorption systems assuming a gas density of  $10^8 \text{ cm}^{-3}$ . Curves as in Fig. 7. The line indicating the model values is thick when it is consistent within 90% with the measured ion ratios, as in Fig. 7. The vertical solid lines mark the allowed  $U$  values in each panel. [See the electronic edition of the Journal for a color version of this figure.]

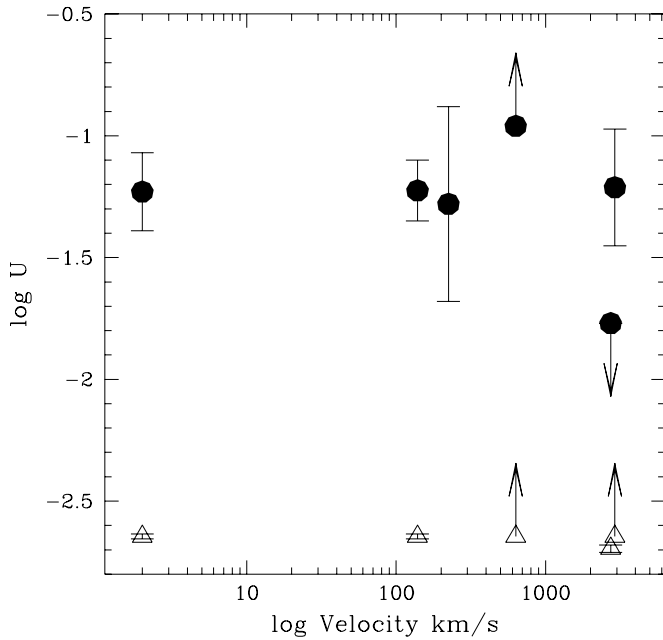


FIG. 9.—Logarithm of the best-fit ionization parameters from Fig. 7 ( $n = 1 \text{ cm}^{-3}$ ; filled circles) and from Fig. 8 ( $n = 10^8 \text{ cm}^{-3}$  [open triangles] shifted by  $\log U = -1.5$ ), as a function of the velocity shift with respect to the redshift of the host galaxy. Error bars and upper limits represent the purely statistical 90% confidence intervals.

the presence of line locking, as first reported by Savaglio et al. (2002). Line locking is usually interpreted as the signature of line radiation pressure acceleration (see, e.g., Foltz et al. 1987; Srianand & Petitjean 2000).

### 3.1.2. The $z = 2.321$ System

For this system (as for  $z = 2.328$  C) we were able to detect C IV and Si IV absorption lines only. The upper limits on the Mg II and Fe II transition allow us to put a significant lower limit on the ionization parameter of  $U \gtrsim 10^{-1}$  for this system for a gas density of  $1 \text{ cm}^{-3}$  and  $U \gtrsim 10^{-1.2}$  for a gas density of  $10^8 \text{ cm}^{-3}$ . For  $n = 1$ , this is higher than the values for the other systems at a confidence level better than 90%. The [C IV/Si IV] ratio is formally inconsistent with this higher ionization parameter, but the disagreement is marginal, taking into account that the C IV/Si IV curves in Figures 7 and 8 are very flat, and therefore small differences in the observed C IV/Si IV ratio would translate into large differences in the ionization parameter. In addition, in this

case the disagreement may be explained by a slight underabundance of C with respect to Si.

### 3.1.3. The $z = 2.296$ and $2.298$ Systems

Given the relatively high velocity shift of about  $3000 \text{ km s}^{-1}$  between the  $z = 2.296$  and  $2.298$  systems and the host galaxy redshift, there is the possibility, at least in principle, that these systems are not associated with the GRB host galaxy but rather are intervening systems. We evaluated the probability of finding intervening C IV systems within  $3000 \text{ km s}^{-1}$  from the GRB host galaxy, from the density distribution of C IV systems given in D'Odorico et al. (1998) and Petitjean & Bergeron (1994). The probability of finding by chance two systems with column densities equal to or larger than those given in Table 5 for these two lowest redshift systems is  $1.2 \times 10^{-5}$ , while the probability for only one of these systems is 0.1% for the  $z = 2.296$  system and 0.5% for the  $z = 2.298$  system.

The  $z = 2.298$  system has an ionization parameter  $< 10^{-1.7}$  at the 90% confidence level for a gas density of  $1 \text{ cm}^{-3}$  (around  $10^{-1.2}$  for a gas density of  $10^8 \text{ cm}^{-3}$ ). This is the lowest of the ionization parameters found in the six systems. Furthermore, for this system we detect a rather strong C II  $\lambda 1334$  ground-state line but not the C II\*  $\lambda 1335$  high-excitation line (see Fig. 5), again indicating a lower radiation field (or a lower gas density).

The observed wavelength of the  $z = 2.298$  system C II  $\lambda 1334$  line coincides with the wavelength of the  $z = 2.296$  C II\*  $\lambda 1335$  line (see Table 3). This may be a further indication of line locking.

### 3.1.4. Intervening Systems

Two main intervening systems are present along the line of sight to GRB 021004, one around  $z = 1.60$  and the other around  $z = 1.38$  (see, e.g., Mirabal et al. 2003; Møller et al. 2003). The UVES high-resolution spectrum of GRB 021004 allows an accurate study of these systems, which are split into several components (see Table 3).

The system at  $z = 1.38$  consists of at least three components at  $z = 1.3807$  ( $z = 1.38$  A),  $z = 1.3802$  ( $z = 1.38$  B), and  $z = 1.3795$  ( $z = 1.38$  C). The latter system is also split in several parts in the range  $1.3793$ – $1.3798$ . The total velocity range spanned by the system is  $\sim 180 \text{ km s}^{-1}$ . We detected the following lines belonging to this system: Si II  $\lambda 1808$ , Al III  $\lambda 1854$ , Fe II  $\lambda 2344$ , Fe II  $\lambda 2374$ , Fe II  $\lambda 2586$ , Mg II  $\lambda \lambda 2796, 2803$ , and Mg I  $\lambda 2852$ .

The system at  $z = 1.60$  comprises at least four components at  $z = 1.6028$  ( $z = 1.60$  A),  $z = 1.6024$  ( $z = 1.60$  B),  $z = 1.6019$  ( $z = 1.60$  C), and  $z = 1.6014$  ( $z = 1.60$  D). The total velocity range spanned by the system is of  $\sim 160 \text{ km s}^{-1}$ . For this system

TABLE 6  
LOGARITHMIC ION COLUMN DENSITIES OF THE GRB 021004 INTERVENING SYSTEMS

System	Velocity Shift ( $\text{km s}^{-1}$ )	Fe II ( $\text{cm}^{-2}$ )	Mg II ( $\text{cm}^{-2}$ )	Si II ( $\text{cm}^{-2}$ )	Al III ( $\text{cm}^{-2}$ )
$z = 1.38$ A.....	0	$15.68 \pm 0.16$	$13.23 \pm 0.07$	$15.12 \pm 0.20$	$13.02 \pm 0.20$
$z = 1.38$ B.....	−63	...	$12.92 \pm 0.32$	...	...
$z = 1.38$ C.....	−150	$14.75 \pm 0.40$	$15.20 \pm 0.70$	...	...
		Fe II	Mg I	Mg II	Al II
$z = 1.60$ A.....	0	$13.69 \pm 0.16$	$11.33 \pm 0.26$	$13.54 \pm 0.21$	$12.66 \pm 0.27$
$z = 1.60$ B.....	−46	$12.63 \pm 0.16$	$11.64 \pm 0.18$	$12.95 \pm 0.10$	...
$z = 1.60$ C.....	−104	$14.35 \pm 0.18$	$12.80 \pm 0.27$	$15.45 \pm 0.80$	$13.24 \pm 0.50$
$z = 1.60$ D.....	−160	$13.57 \pm 0.10$	$11.82 \pm 0.14$	$13.47 \pm 0.06$	$12.58 \pm 0.25$

NOTE.—Errors, upper and lower limits are 90% confidence intervals.

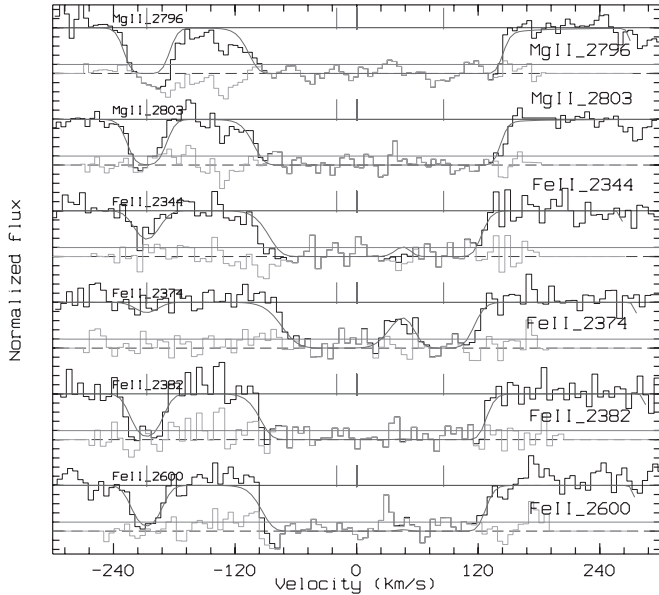


FIG. 10.—UVES spectrum of GRB 020813 near the Fe II  $\lambda 2600$ , Fe II  $\lambda 2382$ , Fe II  $\lambda 2374$ , Fe II  $\lambda 2344$ , Mg II  $\lambda 2803$ , and Mg II  $\lambda 2796$  lines for the three absorption systems, in velocity space, along with the best-fit model (solid line) and residuals (dotted line). The zero of the velocity scale refers to  $z = 1.2545$ . [See the electronic edition of the Journal for a color version of this figure.]

we detected the following lines: Al II  $\lambda 1670$ , Fe II  $\lambda 2344$ , Fe II  $\lambda 2374$ , Fe II  $\lambda 2382$ , Fe II  $\lambda 2586$ , Mn II  $\lambda 2594$ , Fe II  $\lambda 2600$ , Mn II  $\lambda 2606$ , Mg II  $\lambda 2796$ , 2803, and Mg I  $\lambda 2852$ .

We estimated the column densities of the ions of the intervening systems using the same fitting procedure used for the six systems associated with the GRB host galaxy. They are given in Table 6.

### 3.2. GRB 020813

For this GRB we considered the absorption systems at the following velocities with respect to the redshift of the host galaxy, which was assumed to be 1.255 (Barth et al. 2003):  $v = 0$  km s $^{-1}$  (system A in Fig. 10),  $v = -106$  km s $^{-1}$  (system B), and  $v = -306$  km s $^{-1}$  (system C). Note that the system A and system B lines are strongly blended, with the exception of the Fe II  $\lambda 2374$  line. We also consider the system at  $z = 1.2234$ .

We fitted simultaneously the six lines of the three absorption systems in Figure 10. Table 7 gives for the three systems the best-fit Fe II and Mg II abundances along with the velocity shift of each system with respect to the redshift of the host galaxy. Mg II lines of systems A and B are strongly saturated, and therefore their column density estimates are more uncertain. Unfortunately, the UVES spectrum covers a wavelength range much smaller than the Keck LRIS spectrum, and several of the lines studied by Barth et al. (2003) and Savaglio & Fall (2004), in particular Zn II, Cr II, and Si II, are not accessible.

TABLE 7  
GRB 020813 LOGARITHMIC ION COLUMN DENSITIES

System	Velocity Shift (km s $^{-1}$ )	Fe II (cm $^{-2}$ )	Mg II (cm $^{-2}$ )
$z = 1.255$ A.....	0	$15.20 \pm 0.29$	$>16.0$
$z = 1.255$ B.....	-106	$15.47 \pm 0.27$	$>15.5$
$z = 1.255$ C.....	-306	$13.58 \pm 0.10$	$13.79 \pm 0.21$
$z = 1.2234$ .....	-4204	$13.96 \pm 0.18$	$>16.0$

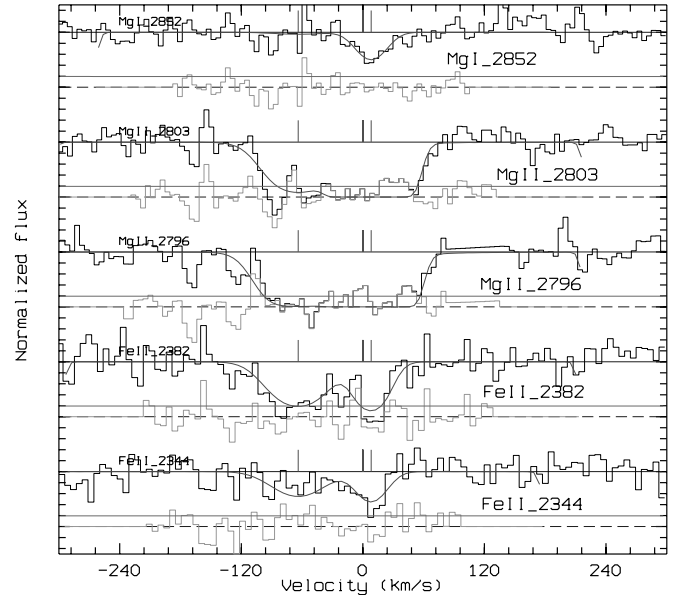


FIG. 11.—UVES spectrum of GRB 020813 near the Fe II  $\lambda 2382$ , Fe II  $\lambda 2344$ , Mg II  $\lambda 2803$ , Mg II  $\lambda 2796$ , and Mg I  $\lambda 2852$  lines for the  $z = 1.2234$  absorption systems, in velocity space, along with the best-fit model (solid line) and residuals (dotted line). The zero of the velocity scale refers to  $z = 1.2234$ . [See the electronic edition of the Journal for a color version of this figure.]

We performed similar fits to the five lines associated with the  $z = 1.2234$  system, split into two components. The results are in Figure 11 and in Table 7. Unfortunately, in this case the redshift of the GRB is not high enough to have strong high-ionization lines in the spectrum, and therefore we do not have a direct way to constrain the ionization status of the gas responsible for the UV absorption.

The [Fe II/Mg II] ratio is consistent with a constant value in the four systems. This ratio is also consistent with meteoritic abundances, assuming that the ionization parameter is in the range  $10^{-2.5}$ – $10^{-1}$ .

### 3.3. The $z = 1.2234$ System

The system at  $z = 1.2234$  is shifted by about 4200 km s $^{-1}$  from the redshift of the host galaxy. The probability of finding an Mg II intervening system with  $W_{\lambda 2796.35} = 1.34 \pm 0.03$  Å (see Table 4) within this velocity range is  $\lesssim 1\%$ , using the distribution of Mg II systems given by Steidel & Sargent (1992). Although not as conclusive as in the case of the  $z = 2.296$  and 2.298 systems in the spectrum of GRB 021004, we remark that this probability is rather small and that the velocity shift with respect to the redshift of the host galaxy is intriguingly similar to that of the GRB 021004 systems.

## 4. DISCUSSION

GRB 021004 shows absorption systems that span  $\sim 3000$  km s $^{-1}$  in velocity toward the observer (no receding system is detected). The systems are most likely local to the GRB, since the probability of finding two or more different absorption systems along the line of sight by random fluctuations is negligible.

It has been suggested that radiative acceleration by the prompt GRB emission may be responsible for the high detected speeds (Schaefer et al. 2003). However, this seems unlikely, since low-ionization ions such Fe II and Mg II are present in the high-velocity absorber. The radiative acceleration is dominated by the GRB and early afterglow radiation. It is therefore unlikely

that recombination can be so rapid as to have any influence on the acceleration of the absorbing material. In the photoionization phase each nucleon receives an amount of energy comparable to the ionization potential of the K shell electron. For a solar metallicity plasma the acceleration is regulated by H atoms, and, at the end of the photoionization, the absorbing material has an outward velocity of

$$v_{\text{ion}} \sim \sqrt{\frac{h\nu_{\text{ion}}}{m_p}} \sim 50 \text{ km s}^{-1}. \quad (1)$$

Once the gas is fully ionized, acceleration proceeds because of radiation pressure on free electrons through inverse Compton (IC) interactions. For a burst of isotropic equivalent energy  $E_{\text{iso}}$  the IC acceleration is obtained by momentum conservation:

$$v_{\text{IC}} = \frac{E_{\text{iso}} \sigma_T}{4\pi R^2 m_p c} \sim 0.6 R_{18}^{-2} \text{ km s}^{-1}; \quad (2)$$

we conclude that at the minimum distance of the absorbing medium  $R \sim 10^{18}$  cm (Lazzati et al. 2002; Heyl & Perna 2003; in order to be ahead of the fireball at the time at which absorption is detected) radiative acceleration is unable to propel the absorber to an outflowing speed comparable to the value(s) observed.

Possible explanations for the large outflowing speed are either a supernova exploded several years prior to the GRB (Vietri & Stella 1998) or a high-velocity wind from the progenitor Wolf-Rayet (WR) star (MacFadyen & Woosley 1999; Schaefer et al. 2003; Mirabal et al. 2003). The large velocity spread with similar ionization parameter is, however, difficult to account for in a supernova remnant (SNR) scenario, where values around a typical expansion velocity would be expected. On the other hand, WR winds are known to be clumpy, and velocities up to  $\sim 4000$  km s $^{-1}$  were detected from P Cygni profiles (Niedzieski & Skórzyński 2002).

In this work we derived physical parameters of the absorbers under the assumption of equilibrium conditions that,  $\sim 0.5$  days after the GRB explosion, are attained only if the electron density in the absorber is  $n \sim 10^7 - 10^8$  cm $^{-3}$ . Assuming equilibrium conditions, the total column density of the absorber can be computed from the ion column density corrected for the ionization fraction. Consider the Si IV line in the A system. The density is given by

$$n = \frac{N_{\text{Si}}}{A_{\text{Si}} R \eta} \sim \frac{10^{15.3}}{4 \times 10^{-5} \times 10^{18} R_{18} \times 10^{-6} \eta_{-6}} \approx 5 \times 10^7 R_{18}^{-1} \text{ cm}^{-3}, \quad (3)$$

where  $R$  is the fireball radius at the time the lines were observed,  $A_{\text{Si}}$  is the Si abundance, and  $\eta$  is the ratio of the width of the absorbing shell over its radius. The ionization parameters derived above and implications discussed here are therefore relevant only in the case of an extremely clumpy wind or SNR.

The photoionization results of CLOUDY yield an ionization parameter constrained in a relatively small range  $10^{-1.7} < U < 10^{-1}$ . In a single-explosion GRB model, the ionization parameter scales with the square of the outflow velocity, since the absorber's distance scales with velocity as well. Even though the ionization parameter depends on the electron density, it seems unlikely that density variations are such as to compensate for the large velocity difference. In a wind environment, on the other

hand, the ionization parameter is constant, since the photon density and particle density scale with the same power of the distance. The relatively small variations in the inferred  $U$ , which do not show any clear trend with velocity, can therefore be interpreted as density fluctuations on top of a regular  $R^{-2}$  wind density profile (as already discussed by, e.g., Schaefer et al. 2003 and Mirabal et al. 2003).

Finally, we note that the Fe II and Mg II column densities found in GRB 020813 are 10–100 times higher than those in GRB 021004. This is likely due to a much higher ionization of the gas in the latter case, rather than a large difference in the total absorbing column of gas or to highly nonsolar metal abundances (note that in both cases the [Fe II/Mg II] ratio is consistent with meteoritic abundances). We also note the similarity between the velocity shift between the  $z = 1.2234$  system and the GRB 020813 host galaxy and the shift of the  $z = 2.296$  and  $2.298$  systems with respect to the GRB 021004 host galaxy. Although the probability for a chance occurrence of the  $z = 1.2234$  system is not as low as in the cases of the two shifted systems in GRB 021004, and the  $z = 1.2234$  ionization status is probably much lower than that of the  $z = 2.296$  and  $2.298$  systems, this similarity might suggest a common scenario for the two GRBs.

## 5. CONCLUSIONS

One of the straightforward results of our UVES high-resolution observations of two GRB afterglows is that the ISM of the host galaxies is complex, and many components contribute to each main absorption system. These components span a total velocity range of up to about 3000 km s $^{-1}$ . Several narrow components are resolved down to a width of a few tens of kilometers per second. The UVES wide band coverage allowed us to investigate simultaneously both high-ionization lines such as C IV and Si IV and low-ionization lines such as Mg II and Fe II in GRB 021004. This allowed us to constrain the ionization parameter of the gas of the different absorption systems. Combined with photoionization results obtained with CLOUDY, the ionization parameters appear to lie in a relatively small range, with no clear trend with the system velocity. This can be interpreted as density fluctuations on top of a regular  $R^{-2}$  wind density profile. The [Mg II/Fe II] ratio of  $\approx 0.4$  found for systems  $z = 2.328$  A,  $z = 2.328$  B, and  $z = 2.298$  is consistent with what is expected from meteoritic abundances. Assuming these abundances, the measured Si IV column density for system  $z = 2.328$  A implies a lower limit of  $\gtrsim 5 \times 10^{19}$  cm $^{-2}$  to the system total hydrogen column density.

Indeed, our study shows that rapid reaction to the GRB triggers and high-resolution and wide spectral coverage are the key ingredients for studying GRB host galaxies. Today observations of this kind are still difficult and rather episodic. However, they should become routine after the launch of the *Swift* satellite, also thanks to the development of a dedicated rapid response observing mode for the VLT telescopes. This mode will make possible automatic follow-up of GRBs (or other transient events) with response times in the 10 minute to 1 hr range, therefore helping in gathering spectra of unprecedented quality of medium- to high-redshift GRB host galaxies.

We acknowledge support from contract ASI/I/R/390/02 and MIUR grant Cofin-2003-41. We thank Fabrizio Nicastro and Emanuele Giallongo for useful discussions, Sandra Savaglio for her early work on this program, and an anonymous referee for comments that helped to improve the presentation.

## REFERENCES

- Akerlof, C., et al. 1999, *Nature*, 398, 400
- Barth, A. J., Sari, R., & Cohen, M. H. 2003, *ApJ*, 584, L47
- Butler, N. R., Marshall, H. L., Ricker, G. R., Vanderspek, R. K., Ford, P. G., Crew, G. B., Lamb, D. Q., & Jernigan, J. G. 2003, *ApJ*, 597, 1010
- Covino, S., et al. 2003, *A&A*, 404, L5
- Dekker, H., D'Odorico, S., Kaufer, A., Delabre, B., & Kotzłowski, H. 2000, *Proc. SPIE*, 4008, 534
- Della Valle, M., et al. 2003, *A&A*, 406, L33
- D'Odorico, V., Cristiani, S., D'Odorico, S., Fontana, A., & Giallongo, E. 1998, *A&AS*, 127, 217
- Ferland, G. S. 2002, *Cloudy 90.04*, Univ. Kentucky Dept. Phys. Astron. Internal Rep.
- Fiore, F., et al. 2002, *GCN* 1524
- Foltz, C. B., Weymann, R. J., Morris, S. L., & Turnshek, D. A. 1987, *ApJ*, 317, 450
- Fontana, A., & Ballester, P. 1995, *ESO Messenger*, 80, 37
- Fox, D. W., Blake, C., & Price, P. A. 2002, *GCN Circ.* 1470
- Fox, D. W., et al. 2003, *Nature*, 422, 284
- Galama, T. J., et al. 1998, *Nature*, 395, 670
- . 1999, *Nature*, 398, 394
- Grevesse, N., & Anders, E. 1989, in *AIP Conf. Proc.* 183, *Cosmic Abundances of Matter*, ed. C. J. Waddington (New York: AIP), 1
- Grevesse, N., Noel, A., & Sauval, A. J. 1993, *A&A*, 271, 587
- Heyl, J. S., & Perna, R. 2003, *ApJ*, 586, L13
- Hjorth, J., et al. 2003, *AJ*, 125, 2291
- Holland, S. T., et al. 2003, *AJ*, 125, 2291
- Lazzati, D., Rossi, E., Covino, S., Ghisellini, G., & Malesani, D. 2002, *A&A*, 396, L5
- MacFadyen, A. I., & Woosley, S. E. 1999, *ApJ*, 524, 262
- Matheson, T., et al. 2003, *ApJ*, 582, L5
- Mirabal, N., et al. 2003, *ApJ*, 595, 935
- Møller, P., et al. 2003, *A&A*, 396, L21
- Nicastro, F., Fiore, F., Perola, G. C., & Elvis, M. 1999, *ApJ*, 512, 184
- Niedźleski, A., & Skórzyński, W. 2002, *Acta Astron.*, 52, 81
- Paczyński, B. 1998, *ApJ*, 494, L45
- Perna, R., & Lazzati, D. 2002, *ApJ*, 580, 261
- Petitjean, P., & Bergeron, J. 1994, *A&A*, 283, 759
- Pettini, M., Smith, L. J., King, D. L., & Hunstead, R. W. 1997, *ApJ*, 486, 665
- Price, P. A., et al. 2003, *Nature*, 423, 844
- Savaglio, S., & Fall, S. M. 2004, *ApJ*, 614, 293
- Savaglio, S., Fall, S. M., & Fiore, F. 2003, *ApJ*, 585, 638
- Savaglio, S., et al. 2002, *GCN* 1633
- . 2004, *ApJ*, 602, 51
- Schaefer, B. E., et al. 2003, *ApJ*, 588, 387
- Silva, A. I., & Viegas, S. M. 2002, *MNRAS*, 329, 135
- Shirasaki, Y., et al. 2002, *GCN* 1565
- Srianand, R., & Petitjean, P. 2000, *A&A*, 357, 414
- . 2001, *A&A*, 373, 816
- Stanek, K. Z., et al. 2003, *ApJ*, 591, L17
- Steidel, C. C., Adelberger, K. L., Giavalisco, M., Dickinson, M., & Pettini, M. 1999, *ApJ*, 519, 1
- Steidel, C. C., & Sargent, W. L. W. 1992, *ApJS*, 80, 1
- Vietri, M., & Stella, L. 1998, *ApJ*, 507, L45
- Villasenor, J., et al. 2002, *GCN* 1471
- Vreeswijk, P. M., et al. 2004, *A&A*, 419, 927
- Woosley, S. E. 1993, *ApJ*, 405, 273